ADVANCED FUNCTIONAL MATERIALS
www.afm-journal.de



# Asymmetric Supercapacitors Based on Graphene/$MnO_2$ Nanospheres and Graphene/$MoO_3$ Nanosheets with High Energy Density

*Jian Chang, Meihua Jin, Fei Yao, Tae Hyung Kim, Viet Thong Le, Hongyan Yue, Fethullah Gunes, Bing Li, Arunabha Ghosh, Sishen Xie, and Young Hee Lee**

**Asymmetric supercapacitors with high energy density are fabricated using a self-assembled reduced graphene oxide (RGO)/$MnO_2$ ($GrMnO_2$) composite as a positive electrode and a RGO/$MoO_3$ ($GrMoO_3$) composite as a negative electrode in safe aqueous $Na_2SO_4$ electrolyte. The operation voltage is maximized by choosing two metal oxides with the largest work function difference. Because of the synergistic effects of highly conductive graphene and highly pseudocapacitive metal oxides, the hybrid nanostructure electrodes exhibit better charge transport and cycling stability. The operation voltage is expanded to 2.0 V in spite of the use of aqueous electrolyte, revealing a high energy density of 42.6 Wh $kg^{-1}$ at a power density of 276 W $kg^{-1}$ and a maximum specific capacitance of 307 F $g^{-1}$, consequently giving rise to an excellent Ragone plot. In addition, the $GrMnO_2$//$GrMoO_3$ supercapacitor exhibits improved capacitance with cycling up to 1000 cycles, which is explained by the development of micropore structures during the repetition of ion transfer. This strategy for the choice of metal oxides provides a promising route for next-generation supercapacitors with high energy and high power densities.**

J. Chang, Dr. M. Jin, F. Yao, T. H. Kim, V. T. Le, Dr. H. Yue, Dr. F. Gunes, B. Li, A. Ghosh, Dr. S. Xie, Prof. Y. H. Lee
IBS Center for Integrated Nanostructure Physics
Institute for Basic Science (IBS)
Daejon, 305-701, Republic of Korea
E-mail: leeyoung@skku.edu
J. Chang, Dr. M. Jin, F. Yao, T. H. Kim, V. T. Le, Dr. H. Yue, Dr. F. Gunes, B. Li, A. Ghosh, Dr. S. Xie, Prof. Y. H. Lee
Department of Energy Science
Department of Physics
Sungkyunkwan University
Suwon, 440-746, Republic of Korea
Prof. S. Xie
Department of Energy Science
Sungkyunkwan University
Suwon, 440-746, Korea
Prof. S. Xie
Institute of Physics
Chinese Academy of Sciences
Beijing, 100190, PR China
Dr. M. Jin
National Center for Nanoscience and Technology
Beijing, 100190, PR China
Dr. H. Yue
School of Materials Science and Engineering
Harbin University of Science and Technology
Harbin, 150040, PR China

DOI: 10.1002/adfm201301851

## 1. Introduction

Energy storage devices, in particular electrochemical capacitors, have attracted tremendous attention for future energy storage applications. Electrochemical capacitors,[1] also known as supercapacitors or ultracapacitors, have been widely used in numerous areas such as hybrid electric vehicles (HEVs), mobile electronic devices, military device and memory backup systems due to their ultra high power density, long cycling stability, wide operation temperature range and improved safety.[2–4] However, they suffer from a lower energy density, which has restricted their potential applications. Therefore, improvement of the energy density of supercapacitors is crucial to meet the future energy demands.[5] The increase of energy (E) can be achieved by maximizing the specific capacitance (C) and the operation voltage (V), $E = 1/2\ CV^2$.[6] For this purpose, Organic electrolyte based symmetric supercapacitors can effectively increase the operation voltage while their low capacitance and unfriendly electrolyte undermine their overall effectiveness for supercapacitor applications.[6,7] On the other hand, aqueous solution is environmentally robust and easy to handle but suffers from narrow operation voltage window of less than 1 V, limiting the use to asymmetric supercapacitors (ASCs). Traditionally, ASCs can make full use of a battery type (faradaic) electrode and a capacitor type (electrochemical double layer) electrode to exhibit two different potential windows in the same electrolyte.[8–10] As a consequence, operation voltage window can be opened and thus the energy density of the supercapacitor could be enhanced significantly.

Among all kinds of electrode materals for ASCs, metal oxides have been investigated extensively since they provide higher specific capacitance and better cycling stability compared to carbon materials and conducting polymers.[11] However, the intrinsic semiconducting nature of metal oxides shows poor electrical conductivity, eventually leading to low power density in ASCs.[12] Graphene, a two dimensional carbon material, is known as a good electrode candidate due to its large surface area, high electrical conductivity, and superior mechanical properties.[13] Previously, Wu and co-workers described ASCs with $MnO_2$ nanowire/reduced graphene oxide composite

(MGC) as a positive electrode and RGO as a negative electrode in 1 M $Na_2SO_4$ aqueous solution.[14] The device exhibited an energy density of 30.4 Wh $kg^{-1}$ at a power density of 5 kW $kg^{-1}$. Although the positive electrode exhibited high capacitance ascribed to the integration of $MnO_2$ nanowires, the restacking of RGO in the negative electrode had influenced the total performance adversely. Currently, Most of reseachers have focused on improving specific surface area (SSA) of graphene, obtaining high SSA in the range of 400–3100 $m^2$ $g^{-1}$, from functionalized graphene,[15] crumpled graphene[16] and activated porous graphene.[17] However, the effective SSA can not be used during charging/discharging (CD) cycles due to the existence of large proportion of micropores and surface incompatibility that are inaccessble by the electrolyte, resulting in low electrochemical double layer capacitance.[18,19] Recently, Wang and co-workers have innovatively developed ASCs with graphene/$Ni(OH)_2$ as a positive electrode and graphene/$RuO_2$ as a negative electrode. A high specific capacitance (153 F $g^{-1}$) and high energy density (48 Wh $kg^{-1}$) at a voltage of 1.5 V in 1 M KOH aqueous solution have been achieved.[20] Unfortunately, the high cost of $RuO_2$ and relatively narrow operation voltage window still hinder their potential industrial applications. Designing and optimizing ASCs for both excellent capacitor-performance and high fabrication-efficiency still remain challenging.

While considerable researches on supercapapcitors aim at increasing energy density and power density, a fundamental working principle of widening operation voltage has been far from being clearly understood. Furthermore, it is highly demanding to lower the fabricating cost and use environmentally friendly materials for practical applications. The work function of metal oxides is directly related to electrochemical oxidation/reduction potential.[21,22] The asymmetric supercapacitor by choosing the largest work function difference of metal oxides can provide a new cell configuration of maximizing operation voltage to accomodate safe neutral aqueous electrolyte. In our work, we designed and fabricated the hybridized nanostructures of reduced graphene oxide (RGO) encapsulated mesoporous $MnO_2$ nanospheres ($GrMnO_2$) for the positive electrode and RGO-wrapped thin layered structure $MoO_3$ nanosheets ($GrMoO_3$) for the negative electrode through a facile self-assembly method. For the positive electrode, mesoporous $MnO_2$ nanospheres exhibit short diffusion path length for both ions of electrolyte and electrons, favoring migration of ions during rapid CD process. For the negative electrode, the thin $MoO_3$ nanosheets support short diffusion path length for ions of electrolyte in the perpendicular direction and continous transport pathways for eletrons in the paralell direction. Finally, the introduction of graphene into two electrodes futher offers extra interface at the hybridized interlayer areas to facilitate charge transport during CD processes, improving the pseudocapacitive reactions and rate capability. Based on the difference of working potential window between $MnO_2$ and $MoO_3$, the hybrid nanostructure ASCs ($GrMnO_2$//$GrMoO_3$) can operate stably up to 2.0 V with a specific capacitance of 307 F $g^{-1}$, reaching an energy density of 42.6 Wh $kg^{-1}$ at a power density of 276 W $kg^{-1}$. Meanwhile, such ASCs also imroved cycling stability up to 1000 cycles with metal oxides wrapped by graphene. Compared to pure metal oxide ASCs ($MnO_2$//$MoO_3$), our hybridized nanostructure ASCs significantly improved both energy density and power density. The hybridized nanostructure electrode materials and cell configuration of the ASC reported here will strongly impact on improving energy density of not only generalized supercapacitors but also solid state flexible supercapacitors with high power density in future.

## 2. Results and Discussion

### 2.1. Principle for the Choice of Metal Oxides

For asymmetric supercapacitor based on the electrodes of two metal oxides, the working potential window can be defined, $E = E_0 + \Delta E_1 + \Delta E_2 = 1 / F (\omega^{\beta} - \omega^{\alpha}) N_A + \Delta E_1 + \Delta E_2$, where $\omega^{\alpha}$ and $\omega^{\beta}$ are the work functions of positive and negative electrodes, respectively; $N_A$ is Avogadro's constant. $\Delta E_1$ and $\Delta E_2$ are the surface dipole potential of positive and negative electrodes, respectively.[21,23,24] For a symmetric electrode, we can assume $\Delta E_1 = -\Delta E_2$ due to the similar charge on positive and negative electrodes and $\omega^{\beta} = \omega^{\alpha}$. In this case, the additional potential window is zero. Thus, operation voltage is determined by the dissociation energy of electrolyte. On the other hand, for an asymmetric capacitor, the work function difference of two metal oxides opens the operation potential, similar to battery operation. Therefore, it is crucial to have two electrode materials with the largest work function difference in asymmetric capacitor. This provides an opportunity of opening the operation voltage even larger than dissociation energy of electrolyte, which is certainly an advantage in terms of increasing energy density efficiently over the symmetric capacitor. For aqueous electrolyte, water dissociation is kinetically limited by hydrogen and oxygen evolution reaction on the surface of metal oxides.

Our strategy is to increase operation voltage window, while maintaining high capacitance of two electrodes in safe aqueous electrolyte (see Table S1). **Figure 1**a shows work functions for various metal oxides.[25–29] It is obvious to choose $MnO_2$ as a positive electrode material and $MoO_3$ as a negative electrode material due to the largest work function difference. For metal oxides with higher work function, Oxygen vacancy defects are more prone to decrease the work function of an oxide because they act as n type dopants, shifting the Fermi level closer to the conduction band edge. The sample was heat-treated to compensate oxygen vacancy in our case and thus high work function value of 6.2 eV is presumably maintained. As for metal oxides with lower work function, especially $MnO_2$ work function of 4.4 eV was maintained due to its environmental stability. The working potential window (1.8 V) can be deduced from the above equation. This determines the operation voltage because the work function difference between electrodes is larger than that of redox potential of aqueous electrolyte. The chemisorption of proton and hydroxide ions on the surface of metal oxides will further extend the potential window by modifying work function of electrode (as shown in Figure 1b). The schematic illustration of the fabricated asymmetric supercapacitor device based on graphene/$MnO_2$ composite as positive electrode and graphene/$MoO_3$ as negative electrode is shown in **Figure 2**.

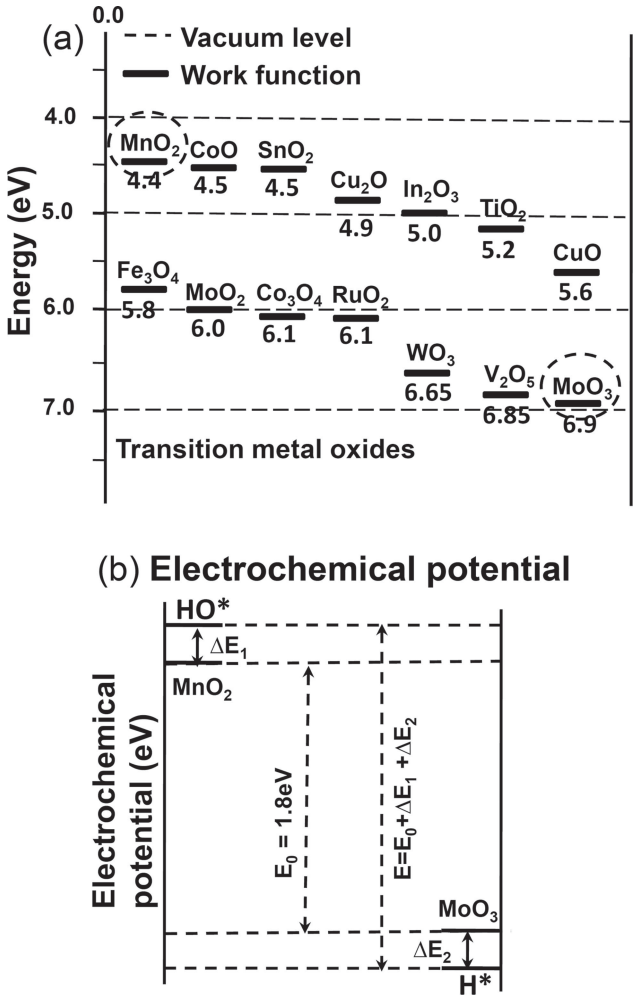


**Figure 1.** a) Schematic illustration of work function of different metal oxides. b) Relationship between potential window and the shift of work function (electrochemical potential) of two electrodes during charging.

### 2.2. Characterizations of Positive Electrode Materials

The morphologies and detailed structures of pure $MnO_2$ and $GrMnO_2$ composites were characterized by both FESEM and TEM observations. **Figure 3**a shows the $MnO_2$ nanospheres whose average diameters are around 300–400 nm. Based on the low and high magnification TEM images of $GrMnO_2$ composites (Figure 3b and c), the $MnO_2$ nanospheres are wrapped and loosely interconnected by RGO, which ensures easy transport of electrons through highly conductive graphene channels. Figure 3d shows the typical X-ray diffraction (XRD) patterns of the $GrMnO_2$ composite and pure $MnO_2$. All of the peaks of two samples can be indexed as the tetragonal α-$MnO_2$ phase (JCPDS No. 44-0141).[30] It should be noted that $GrMnO_2$ composites exhibit better crystalline nature than pure $MnO_2$ after reduction of graphene oxide. Figure 3e shows Raman spectra of α-$MnO_2$, approximately near 640 $cm^{-1}$, which belongs to Ag mode originating from breathing vibration of $MnO_6$ octahedra.[31] The Raman bands at 1360 $cm^{-1}$ and 1600 $cm^{-1}$ are assigned to the D band and G band of RGO, respectively. The D band corresponds to the breathing mode of rings or k point phonons of $A_{1g}$ symmetry, whereas the G band represents the in-plane bond-stretching motion of the pairs of $sp^2$ carbon atoms ($E_{2g}$ phonons).[32] The Fourier transformed infrared (FTIR) spectrum of as-prepared sample is shown in the range of 500–4000 $cm^{-1}$ (please, see Figure S2).

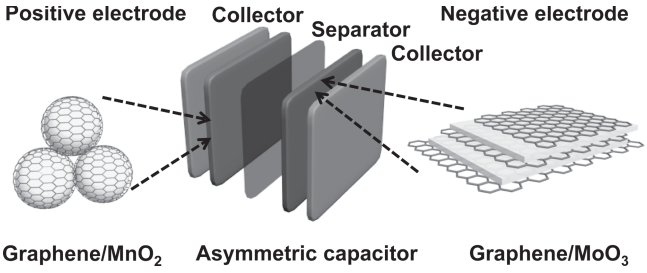


**Figure 2.** Schematic illustration of the fabricated asymmetric supercapacitor device based on graphene/$MnO_2$ composite as positive and graphene/$MoO_3$ as negative electrode in a neutral aqueous $Na_2SO_4$ electrolyte.

The graphene oxide was effectively reduced to graphene with some remaining carboxyl groups. In order to confirm the specific surface area and porous structure, we measured the liguid nitrogen cryosorption of as-prepared $GrMnO_2$. The nitrogen adsorption and desorption isotherm shows typical II/IV characteristics (Figure 3f),[14] indicating that the pores constructed by RGO and $MnO_2$ nanospheres are more mesoporous and less microporous with a corresponding specific surface area of 152 $m^2$ $g^{-1}$. We also caculated the micropore and mesopore size distribution based on the Horvath-Kawazoe (HK) and Barrett Joyner Halenda (BJH) methods, respectively (inset of Figure 3f). The maximum peak was shown near 4.0 nm. As a consequence, the $GrMnO_2$ composite structure is favorable for improving both the main pseudocapacitance of α-$MnO_2$ and the electrochemical double layer capacitance of RGO since hydrated ions in electrolyte are easily accessible to this structure with high surface area and mesopores.

Cyclic voltammetry (CV) is generally used to characterize the capacitive behavior of an eletrode material. **Figure 4**a shows the typical CV curves of as-prepared $GrMnO_2$ and pure $MnO_2$ at a scan rate of 20 mV $s^{-1}$ using 1M $Na_2SO_4$ solution. Compared to that of pure $MnO_2$, CV curve of RGO/$MnO_2$ shows higher capacitance and relatively more rectangular in shape than $MnO_2$, approching the ideal capacitive behavior. This is ascribed to the highly conductive graphene wrapped on the surface of $MnO_2$ nanospheres. The specific capacitance of the electrode ($C_s$) can be calculated according to the following equation, $C_S = \frac{(|Q_A|+|Q_C|)}{[m\times(2\times\Delta V)]}$, where $|Q_A|$ and $|Q_C|$ are the charges stored in the anode and cathode, respectively.[33] The mass of working electrode is m and the potential window of the CV curve is expressed as ΔV. The specific capacitances of $GrMnO_2$ and pure $MnO_2$ are plotted as a function of scan rate in Figure 4b. $GrMnO_2$ composite exhibits higher rate performance than pure $MnO_2$ particualrly at higher scan rate, which is contributed from extra interface at the hybridized interlayer areas.

Figure 4c shows that the galvanostatic CD curves of the $GrMnO_2$ composite are almost linear and symmetrical without an obvious IR drop, indicating a rapid I-V response and

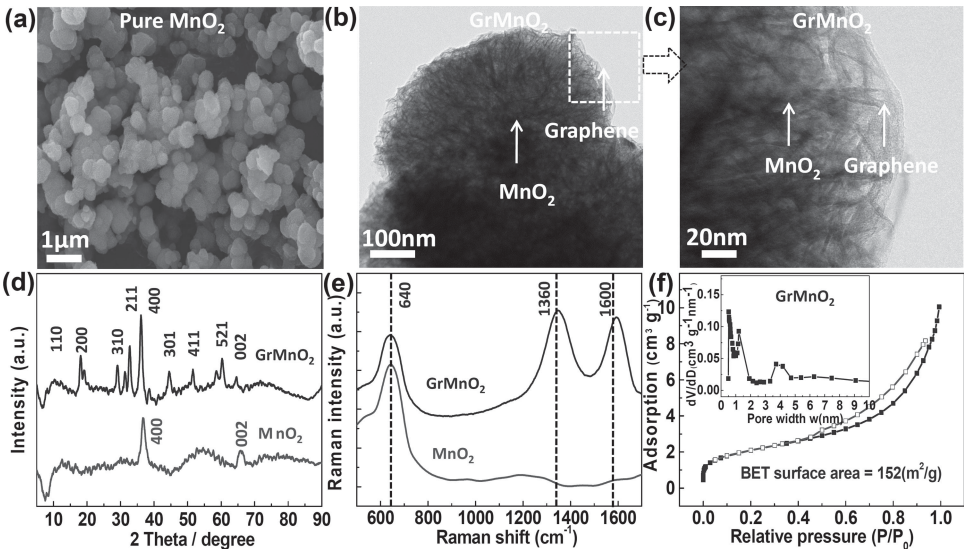


**Figure 3.** a) SEM image of pure $MnO_2$ exhibits flower-like morphology. b) Low and c) high magnification TEM images of $GrMnO_2$ composite showing graphene coating the particles of flower-like $MnO_2$. d) XRD patterns of pure $MnO_2$ and graphene/$MnO_2$. e) Raman spectra of the pristine $MnO_2$ and $GrMnO_2$ composite. f) $N_2$ adsorption/desorption isotherms of $GrMnO_2$ composite at 77 K ( the inset of (d) exhibits micropore and mesopore size distributions obtained from $N_2$ adsorption isotherms (77 K) of $GrMnO_2$ samples by the HK and BJH methods).

significant enhancement of the composite conductivity and excellent reversibility. Figure 4d presents the specific capacitance obtained from galvanostatic CD curves of the $GrMnO_2$ composite and pure $MnO_2$. The $GrMnO_2$ composite exhibits higher capacitance at higher current density compared to pure $MnO_2$. $GrMnO_2$ composite with 10 wt% graphene exhibits high specific capacitances of 350 F $g^{-1}$ and 162 F $g^{-1}$ at a current density of 200 mA $g^{-1}$ and 10 A $g^{-1}$, respectively. The enhancement of specific capacitance and rate capability of the composite can be attributed to the key two factors: i) mesoporous $MnO_2$ nanospheres which exhibit short diffusion path lengths for both electrolyte ions and electrons, favoring fast diffusion of electrolyte ions during CD process and ii) graphene acts as better electron transport channel and offers better interconnectivity among $MnO_2$ nanoparticles than pure $MnO_2$. This futher provides electrochemical double layer capacitance to increase total capacitance. Meanwhile, the chemically synthesized graphene with abundant defects is favorable for ions diffusion into the core–shell unit structure.[34,35]

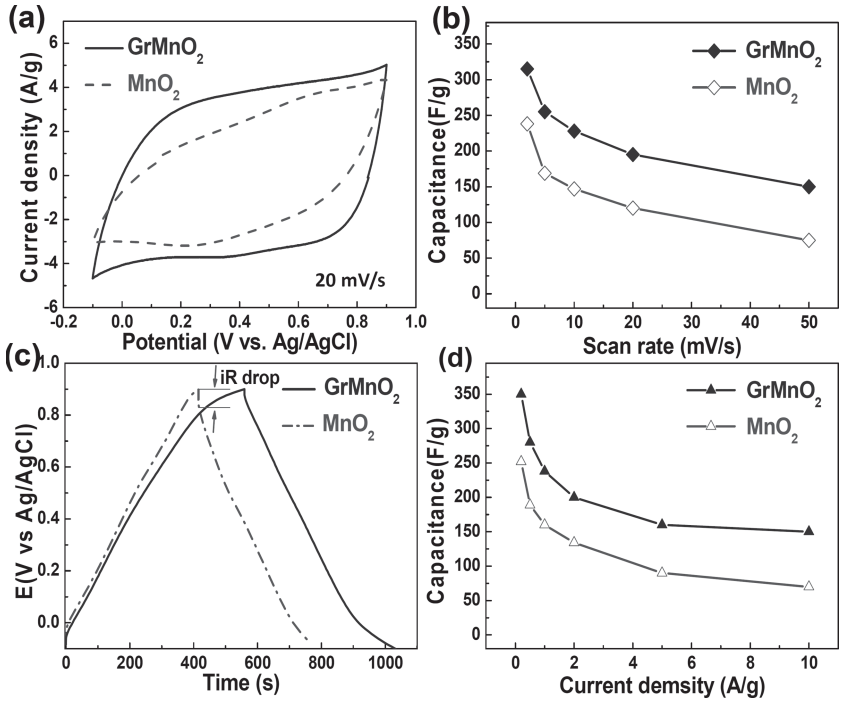


**Figure 4.** a) CV curves of pure $MnO_2$ and $GrMnO_2$ composite at 20 mV $s^{-1}$ in 1 M $Na_2SO_4$ electrolyte. b) Specific capacitances of pure $MnO_2$ and $GrMnO_2$ composite at different scan rates. c) Galvanostatic charge/discharge curves of pure $MnO_2$ and $GrMnO_2$ composite at a current density of 500 mA $g^{-1}$. d) Specific capacitance of pure $MnO_2$ and $GrMnO_2$ composite as a function of the current densities calculated from the corresponding discharge curve for each current density.

### 2.3. Characterizations of Negative Electrode Materials

In spite of abundant researches done on positive electrodes, studies on the negative electrode materials with transition metal oxides have been limited due to the unsatisfactory capacitive performance or high cost of several types of electrode materials.[36] $\alpha$-$MoO_3$ is low cost and layer-structured material, which facilitates the injection of different electrolyte ions into the free spaces, thus creating better electrochemical properties.[37,38] Therefore, we tried to explore electrochemical reaction

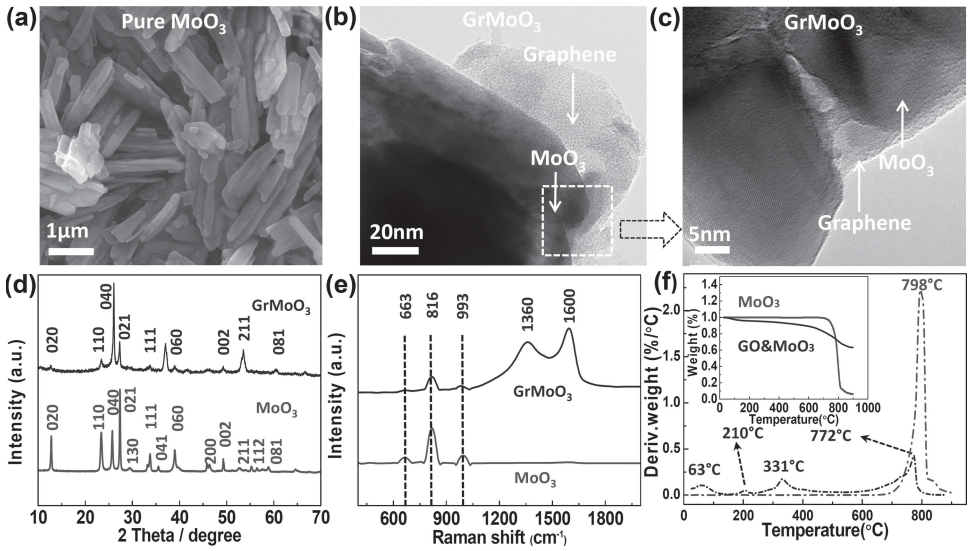


**Figure 5.** a) SEM image of pure $MoO_3$ exhibits nanosheets morphology. b) High magnification TEM images of $GrMnO_2$ composite showing graphene wrapping $MoO_3$ nanosheets. c) XRD patterns of pure $MoO_3$ and $GrMnO_2$. d) Raman spectra of the pristine $MoO_3$ and $GrMoO_3$ composite. f) Differential thermogravimetric curves of $MoO_3$ and Graphene oxide wrapping $MoO_3$ (GO & $MoO_3$) at the atmosphere of $N_2$ (the inset of (d) exhibits the corresponding thermogravimetric curves).

of α-$MoO_3$, which is proved to be a very suitable negative electrode with high capacitance characteristics.

The corresponding detailed structures of pure $MoO_3$ and RGO/$MoO_3$ composites were also individually characterized by both FESEM and TEM, as shown in **Figure 5**. The prepared pure $MoO_3$ consists of 2-dimensional nanosheets whose thickness is on the average about 100 nm and size is about 2 μm (Figure 5a). After self-assembly of RGO with $MoO_3$ nanosheets, the detailed structure of the composite was confirmed using low and high magnification TEM. The results show that $MoO_3$ nanosheets are uniformly distributed on the surface of graphene layers. The combination of RGO and $MoO_3$ nanosheets enhanced the ability to transport electrons. Figure 5d shows the typical XRD patterns of the $GrMoO_3$ composite and pure $MoO_3$. The pure $MoO_3$ presents very sharp diffraction peaks of $MoO_3$ (JCPDS No.05-0508), which indicates a highly crystalline orthorhombic structure (α-$MoO_3$).[39] However, the (040) peak of $GrMoO_3$ is much stronger than pure $MoO_3$, indicating that the layer perpendicular to [010] direction is lying parallel to the plane of graphene layer, thus enhancing packing of $MoO_3$ sheets on graphene.[39,40] Figure 5d shows the Raman spectrum of as-synthesized $GrMoO_3$ and pure $MoO_3$ in the frequency range of 400–1950 $cm^{-1}$. Three main peaks at 993, 816, 663 $cm^{-1}$ further confirm the α-$MoO_3$ orthorhombic structure.[41] The D band and G band at 1360 $cm^{-1}$ and 1600 $cm^{-1}$ for the $GrMoO_3$ composite confirm the existence of graphene. The FTIR spectrum also shows the removal of functional groups on the surface of graphene layer, such as –OH, C–O–C or C=O functional groups (see S1). Thermal stability of graphene oxide/$MoO_3$ and pure $MoO_3$ was investigated by using the thermogravimetric analysis (TGA). As shown in the inset of Figure 5f, the graphene oxide/$MoO_3$ shows the regular weight loss on the TGA curve. Three characteristic peaks with a shoulder on the differential TGA (DTGA) curve (Figure 5f) were observed at about 63, 210, 331 °C. The peaks of before 100 °C were attributed to the removal of the adsorbed water while the sharp peak at 210 and 331 °C corresponded to the removal of the oxygen functional groups, generating the CO and $CO_2$.[42] Our sample was annealed at 400 °C for 2 h to remove oxygen functional groups, allowing the lowest temperature to protect against the structural change of $MoO_3$ nanosheets.

The electrochemical tests of the electrode materials were performed in a three-electrode cell using aqueous 1 M $Na_2SO_4$ electrolyte. $GrMoO_3$ exhibits better electrochemical performance than pure $MoO_3$ with a working potential window of –1.0 to 0 V (vs. Ag/AgCl). Graphene/$MoO_3$ with 10 wt% graphene exhibits a higher specific capacitance of 291 F $g^{-1}$ at 2 mV $s^{-1}$, much better than carbon materials. The rate capability of $GrMoO_3$ is also better than that of $MoO_3$ owing to the improvement of electrical conductivity, as shown in **Figure 6**b. However, poor electrical conductivity of $MoO_3$, high active loading (90 wt%), and relatively thick film of electrode (20 μm) gave rise to slow pseudocapacitance reaction at high scan rate. The high specific capacitance is ascribed to two factors: i) Thin $MoO_3$ nanosheets support short diffusion path lengths for electrolyte ions in the perpendicular direction and continous transport pathways for eletrons in the paralell direction. and aslo potentially tailor the distance between each graphene layer to allow more electrolyte ions to penetrate into the nanostrucutre electrode. ii) The graphene in composite is intertwined and intimately bound with $MoO_3$ nanosheets, serving dual functions as both conductive channels and active interface centers. Graphene offers better interconnectivity between $MoO_3$ nanosheets and furthermore participates in electrochemical double layer capacitance.

### 2.4. Hybridized Nanostructure Asymmetric Supercapacitor

Considering high capacitance of the redox characteristics and fast ion transport properties of $GrMnO_2$ and $GrMoO_3$

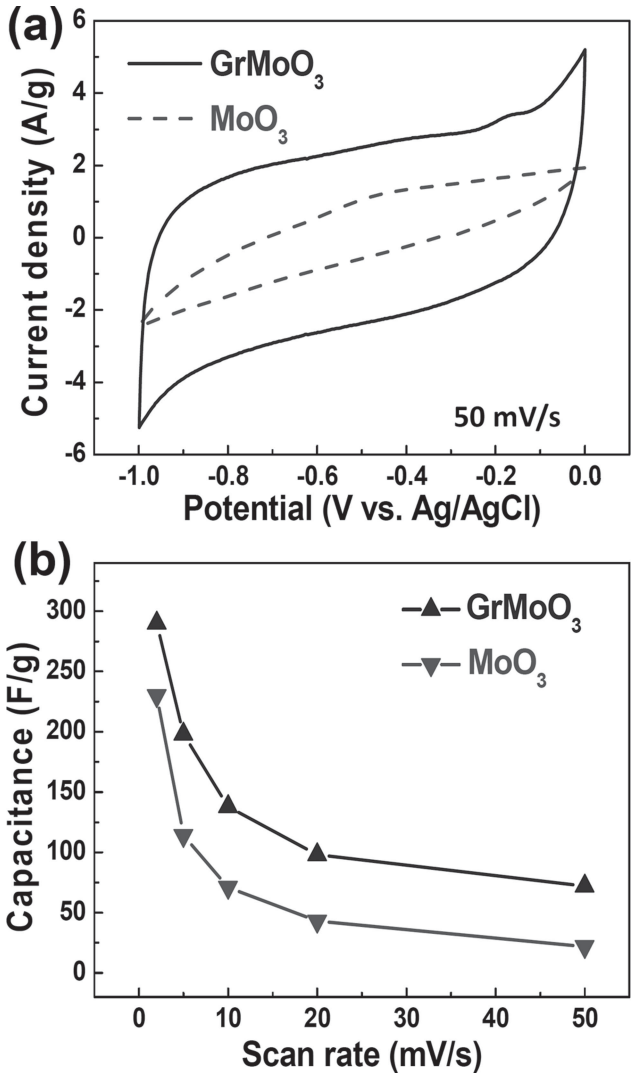


**Figure 6.** a) CV curves of pure $MoO_3$ and $GrMoO_3$ composite at 50mV $s^{-1}$ in 1 M $Na_2SO_4$ electrolyte. b) Specific capacitances of pure $MoO_3$ and $GrMoO_3$ composite at different scan rates.

composite, an asymmetric supercapacitor was fabricated using these materials as the positive and negative electrodes, respectively. To further evaluate the electrochemical properties and estimate the stable potential windows of $GrMnO_2$ and $GrMoO_3$ prior to evaluation of the asymmetric unit cell, we performed CV measurements on the two electrode materials in 1 M $Na_2SO_4$ aqueous solution, using a three-electrode cell with a platinum mesh as an auxiliary electrode and a Ag/AgCl (saturated NaCl) electrode as a reference electrode. The $GrMnO_2$ electrode was measured at a scan rate of 5 mV $s^{-1}$ within a potential window of −0.1 to 0.9 V(Ag/AgCl), while $GrMoO_3$ was measured within a potential window of −1.0 to 0 V (Ag/AgCl) (**Figure 7**a). The specific capacitance calculated from the CV curve at a scan rate of 5 mV $s^{-1}$ was 255 F $g^{-1}$ for $GrMnO_2$ composite and 198 F $g^{-1}$ for $GrMoO_3$ composite, respectively. The specific capacitance of the composites was derived from the combined contribution of redox pseudocapacitance of metal oxide and electrochemical double layer capacitance of graphene in the composites. By expressing the total cell voltage as the sum of the potential range of $GrMnO_2$ and $GrMoO_3$, the hybridized nanostructured ASCs can be operated up to 1.9 V. Because more negative potential and positive potential can be achieved, both hydrogen and oxygen evolution reactions are supposed to be kinetically limited on these transition metal oxide and graphene composites.[7,43] As a consequence, the operation voltage window can be extended from −0.1 to 1.2 V vs. Ag/AgCl for $MnO_2$ nanospheres and from −1.3 to 0.2 V for $MoO_3$ nanosheets in 1M $Na_2SO_4$ electrolyte. In this way, we can still avoid the decomposition of aqueous electrolyte under an operation voltage 2.0 V, reaching a safe performance of both electrodes during long cycling.

As for ASCs, the charge balance will follow the relationship $q_+ = q_-$ ($q_+$ is the positive electrode charge and $q_-$ is the negative electrode charge).[9] The charge stored by each electrode depends on the specific capacitance (C), the potential window (ΔE) during the charge/discharge process and the mass of the electrode (m) following: $q = C \times \Delta E \times m$, and in order to get $q_+ = q_-$, the mass balance, $\frac{m_+}{m_-} = \frac{C_- \times \Delta E_-}{C_+ \times \Delta E_+}$. On the basis of the specific capacitance values and potential windows of the $GrMnO_2$ and $GrMoO_3$ composite, the optimized mass ratio of $\frac{m_{GrMnO_2}}{m_{GrMoO_3}}$ should be 0.78 in the ASC cell.

Figure 7b shows the CV curves of an optimized ASC full cell measured at different scan rates between 0 and 2.0 V in 1 M $Na_2SO_4$ electrolyte. These CV curves exhibit distorted rectangular shapes indicating both pseudocapacitance and EDLC contributions. To further evaluate the performance of unit cell, we measured galvanostatic CD curves at various current densities (Figure 7c). The non-linearity in the discharge curves particularly at lower current density indicates some contribution of the redox reaction from metal oxides, in congruent with CV curves. The specific capacitance of one electrode has been evaluated from the CD curves according to the following equation: $C_{sp} = \frac{4C}{M} = \frac{4I}{M(-\frac{dV}{dt})}$, where I is the applied discharging current, M is the total mass of positive and negative electrodes and dV/dt is the slope of discharge curves. A specific capacitance of 307 F $g^{-1}$ is obtained at a current density of 200 mA $g^{-1}$ (Figure 7d), which is attributed to the combination of high specific capacitances in both electrodes.

Long cycle life is an important requirement for supercapacitor. The cycle life test during 1000 cycles for $GrMnO_2$//$GrMoO_3$ ASCs was carried out by repeating the CV test between 0 and 2.0 V at a scan rate of 50 mV $s^{-1}$. **Figure 8**a shows the capacitance as a function of cycle number. It is worth noting that the specific capacitance sharply increases at the initial 100 cycles, which is probably related to an improvement in the surface wetting of the electrode by electrolyte and activation of the active materials. This can be rationalized by hydrophobic nature of graphene. During the following cycles, the ASC displays an excellent cycling stability with a little deterioration. The cycling stability can be ascribed to the hybridized nanostructures of two electrodes: The core-shell $GrMnO_2$ structure effectively prevents the $MnO_2$ nanospheres from being dissolved into electrolyte by graphene wrapping. In general, $Mn^{4+}$ in $MnO_2$ can be converted into $Mn^{3+}$ and $Mn^{2+}$ and these ions will flow through the separator to the negative electrode, resulting in decreasing the capacitance of both electrodes during CD process.[44] $GrMoO_3$ layer stacking structure is also attributed to prevent $MoO_3$ from being dissolved into electrolyte.

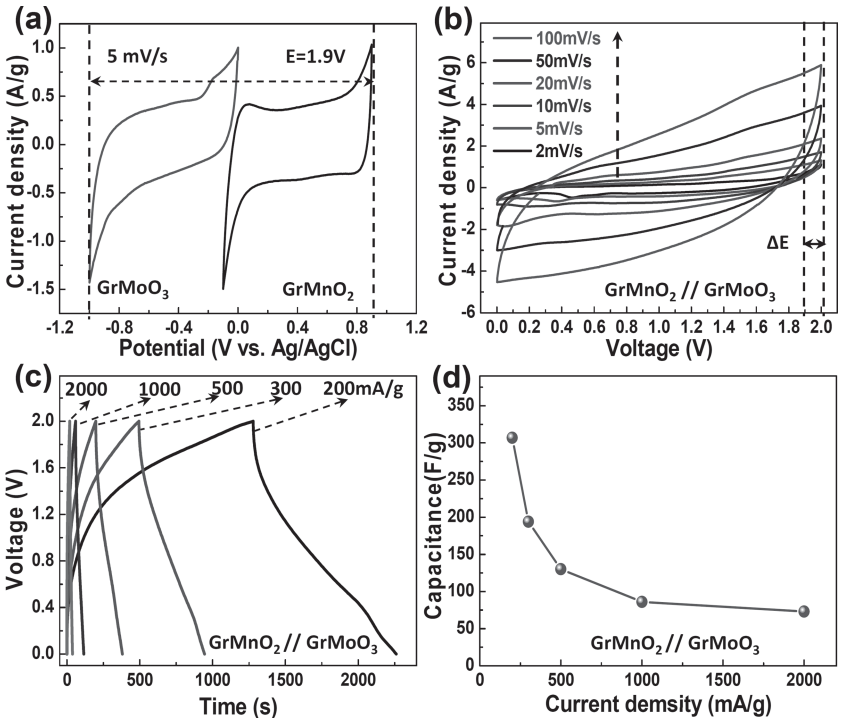


**Figure 7.** a) Comparative CV curves of $GrMnO_2$ and $GrMoO_3$ electrodes performed in three-electrode cell in 1 M $Na_2SO_4$ electrolyte at a scan rate of 5 mV $s^{-1}$. b) CV curves an optimized graphene/$MnO_2$//graphene/$MoO_3$ asymmetric supercapacitor at different scan rates 1M $Na_2SO_4$ electrolyte. c) Galvanostatic charge/discharge curves of $GrMnO_2$//$GrMoO_3$ asymmetric supercapacitor at different current densities. d) Specific capacitance of one electrode in the asymmetric supercapacitor at different current densities.

Figure 8b shows Ragone plot for energy density and power density. The specific energy density (E, Wh $kg^{-1}$) and power density (P, W $kg^{-1}$) for a supercapacitor cell can be calculated using the following equations: $E = 1/2\ CV^2$ and $P = E/t$, where C is the specific capacitance of supercapacitor cell, V is voltage change during the discharge process after IR drop in V-t curve, and t is the discharge time. Figure 8b shows the Ragone plots of the supercapacitors calculated from Figure 7d. It is more reasonable to choose CD measurements to calculate energy density and power density for evaluating practical application of supercapacitors instead of CV measurements. The $GrMnO_2$//$GrMoO_3$ ASCs with a cell voltage of 2.0 V can exhibit an energy density of 42.6 Wh $kg^{-1}$ at a power density of 276 W $kg^{-1}$. In comparison, $MnO_2$//$MoO_3$ ASCs were also fabricated for reference. The hybridized nanostructure ASCs exhibit better electrochemical performance, which can be attributed to the integration of graphene into two electrodes, improving the pseudocapacitance of metal oxides. The hybridized nanostructure ASCs also exhibit much higher energy density than other reported ASCs, such as $MnO_2$//AC,[45] NiO//Porous carbon,[46] and Graphene/$MnO_2$ nanowires//graphene.[14] The energy density is much higher than those of noble metal oxides based ASCs, such as CNT/$MnO_2$//CNT/$In_2O_3$ (25.5 Wh $kg^{-1}$),[7] RGO/$RuO_2$//RGO/PANi (26.3 Wh $kg^{-1}$).[47] The enhancement of energy density here is attributed to the enlarged operation voltage and the increased specific capacitance of both electrodes. The electrochemical performance could be improved by further optimizing structures of metal oxides and combination with doped graphene layers.

Our hybridized nanostructure ASCs of integration of metal oxides with graphene present much better performance than $MnO_2$//$MoO_3$ ASCs. To further examine the fundamental electrochemical behavior of ASCs, the electrochemical impedance spectroscopy (EIS) analysis has been introduced to measure the impedance in the frequency range of 10 mHz–100 kHz at open circuit potential with an ac perturbation of 10 mV (**Figure 9**a). The Nyquist plots obtained were modeled and interpreted with the help of an appropriate electric equivalent circuit (Figure 9b and c), where Re stands for a combined resistance of ionic resistance of electrolyte, intrinsic resistance of substrate and contact resistance at the active material/current collector interface, Rct the charge tansfer resistance casued by the faradaic reaction, W1 the Warburg type element related to electrolyte ions diffusion, CPE the constant phase element, C1 the double layer capacitance and C2 the limit capacitance.[9,48] It is clear to see that the integration of graphene into both electrodes decreases contact resistance with electrolyte, charge transfer resistance and electrolyte diffusion resistance compared to the electrodes of pure metal oxides (as shown in S3). An impedance phase angle plot is also shown in Figure 9d. The "knee frequency" of the ASC is about 1.8 Hz at a phase of –45°, which exhibits a pure capacitive behavior.[49] Most of its stored energy is accessible at frequencies below 1.8 Hz. The phase angle of the supercapacitor was about –80° at a frequency of 10 mHz, close to –90° for ideal capacitors, coinciding with the electric equivalent circuit for the ASC. Compared with previously and recently reported ASCs (as shown in Table 1),[7,9,14,15,17,20,45,50–56] our ASC shows higher energy density at an operation voltage of 2.0 V in a neutral aqueous $Na_2SO_4$ electrolyte. Even though our hybridized nanostructure ASCs exhibit lower power density than textiles based supercapacitor,[57] we will be able to combine these different metal oxides with graphene foam or high conductive textiles in ASCs for further improving the performance in future.

## 3. Conclusions

We have successfully developed an ASC using graphene/$MnO_2$ composite and graphene/$MoO_3$ composite as positive and negative electrode, respectively that operates at large operation voltage window. The ASC shows high specific capacitance, high energy density, and good cycling stability at an operation voltage window of 2.0 V in neutral aqueous $Na_2SO_4$ electrolyte. We proved that it is highly desirable for coupling the graphene/$MnO_2$ composite with the graphene/$MoO_3$ composite to produce supercapacitors with high energy demands. Such

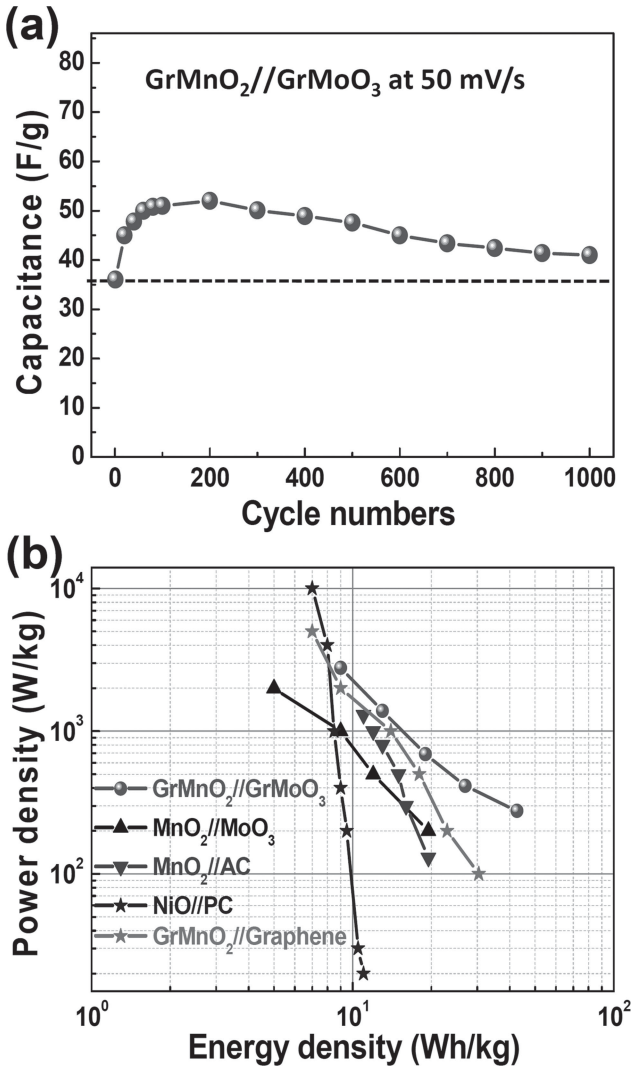


**Figure 8.** a) Cycle performance of the optimized $GrMnO_2//GrMoO_3$ asymmetric supercapacitor within a voltage window of 2.0 V at a scan rate of 50 mV $s^{-1}$. b) Ragone plot related to energy and power densities of the $GrMnO_2//GrMoO_3$ asymmetric supercapacitor operated at 2.0 V in comparison to $MnO_2//MoO_3$ asymmetric Supercapacitor, $MnO_2$ /AC, NiO// Porous carbon, and Reduced graphene oxide/$MnO_2$ nanowires//Reduced graphene oxide ($GrMnO_2$//Graphene) recently reported in the literature.

hybridized nanostructure ASCs presented here aims at lowering fabricating cost and using environmental friendly materials for practical applications. The electrode materials and cell configuration of the ASC provide a promising research direction for the next generation, green and low-cost supercapacitors with high energy density and power storage demands.

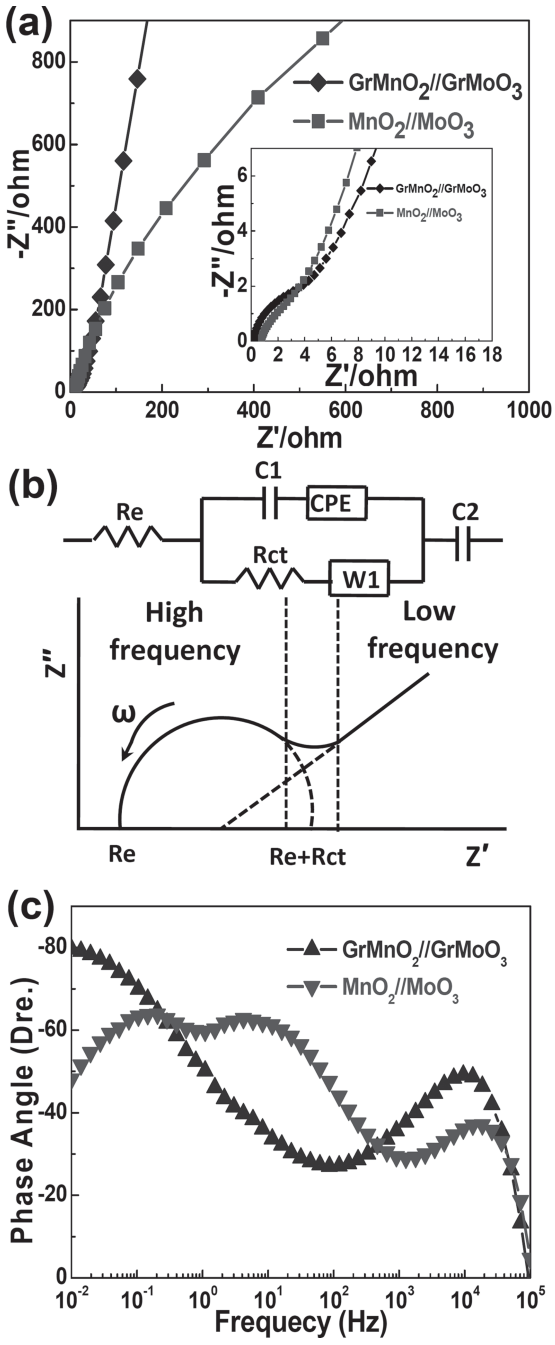


**Figure 9.** a) Nyquist plots of $GrMnO_2//GrMoO_3$ and $MnO_2//MoO_3$ Asymmetric supercapcitors (the inset of (a) exhibits high frequency region Nyquist plots). b) Modeled equivalent circuit of electrochemical impedance spectroscopy (EIS). c) Schematic of EIS. d) Phase angle for $GrMnO_2//GrMoO_3$ and $MnO_2//MoO_3$ Asymmetric supercapcitors measured in frequency range of 100 kHz to 0.01 Hz.

## 4. Experimental Section

### 4.1. Sample Preparation

*Synthesis of Graphene/$MnO_2$ Nanosphere Composite*: Graphite oxide was synthesized from graphite powder according to the modified Hummers method and purified by a two-step acid-acetone wash to remove the salt byproducts.[58,59] Then graphene oxide dispersion (0.5 ml $mg^{-1}$) was prepared after 0.5 h sonication. $MnO_2$ nanospheres were prepared by a simple chemical coprecipitate method according to the previous report.[60] To wrap graphene oxide on the surface of $MnO_2$ nanospheres, 200 mg $MnO_2$ were dispersed into 100 mL ethanol and sonicated for 0.5 h, and then 1 mL 3-aminopropyltriethoxysilane (APTMS) was added and refluxed for 4 h at 50 °C water bath. After reaction, filtering and rinsing

**Table 1.** Performances comparison of ASCs with positive and negative electrodes fabricated by different methods.

| ASCs structure | Method | Electrolyte | Operation voltage [V] | Energy density [Wh $kg^{-1}$] | Power density [W $kg^{-1}$] | Cycle number | Ref |
|---|---|---|---|---|---|---|---|
| $Ni(OH)_2$/CNT/NF//AC | Chemical bath deposition | KOH | 1.8 | 50.6 | 95 | 3000 | [50] |
| $NaMnO_2$//AC | Ball milling | $Na_2SO_4$ | 1.9 | 19.5 | 130 | 10000 | [55] |
| $MnO_2$//Mesoporous CNT | Chemical precipitation | $Na_2SO_4$ | 2.0 | 47.4 | 200 | 1000 | [51] |
| Graphene/$MnO_2$//Graphene | Solution mixing | $Na_2SO_4$ | 2.0 | 30.4 | 100 | 1000 | [14] |
| Graphene/$MnO_2$//ACF | Microwave | $Na_2SO_4$ | 1.8 | 51.1 | 198 | 1000 | [9] |
| $MnO_2$//Graphene hydrogel | Electro-deposition | $Na_2SO_4$ | 2.0 | 23.2 | 1000 | — | [15] |
| Activated graphene/$MnO_2$//Activated graphene | Self-reaction deposition | $Na_2SO_4$ | 2.0 | 32.3 | 21 | 5000 | [17] |
| Graphene/PANi//Graphene/$RuO_2$ | Chemical synthesis | KOH | 1.4 | 26.3 | 150 | — | [47] |
| $TiO_2$//CNT | Hydrothermal reaction | $LiPF_6$ | 2.8 | 12.5 | 300 | 600 | [52] |
| Graphene/$Ni(OH)_2$//Graphene/$RuO_2$ | Chemical synthesis | KOH | 1.5 | 48.0 | 230 | 5000 | [20] |
| Carbon spheres/$MnO_2$//Carbon spheres | Self reaction deposition | $Na_2SO_4$ | 2.0 | 22.1 | 100 | 1000 | [53] |
| $MnO_2$//FeOOH | Hydrolysis | $Li_2SO_4$ | 1.85 | 24.0 | 450 | 2000 | [54] |
| $K_{0.27}MnO_2$//Activated carbon | Ball milling | $K_2SO_4$ | 1.8 | 25.3 | 140 | 10000 | [45] |
| CNT/$MnO_2$//CNT/$In_2O_3$ | Filtering | $Na_2SO_4$ | 2.0 | 25.0 | — | — | [7] |
| Ni-Zn-Co oxide/hydroxide//Porous carbon | Chemical synthesis | $Na_2SO_4$ | 1.5 | 41.6 | 100 | 1000 | [56] |
| Graphene/$MnO_2$//Graphene/$MoO_3$ | Self-assembly | $Na_2SO_4$ | 2.0 | 42.6 | 276 | 1000 | Present |

were done by adding more ethanol. Finally, 200 mg APTMS treated $MnO_2$ particles were dried at 70 °C for 2 h, and then put into 100 mL water solution (pH = 6) and sonicated for 30 min further. Then 20 ml graphene oxide dispersion (0.5 mL $mg^{-1}$) was added into the above solution and stirred for 30 min. Finally 0.5 ml $N_2H_4$ (80%) was used to reduce the graphene oxide by stirring the mixture at 90 °C for 4 h.

*Synthesis of Graphene/$MoO_3$ Nanosheet Composite*: For synthesis of $MoO_3$ nanosheets, 1.2 g molybdenum powder was placed into a flask, and then 10 mL $H_2O_2$ (30%) was added into the flask slowly during stirring under an ice bath. After the solution was turned into transparent yellow, the solution was aged at room temperature for 12 h to get a sol and then the sol was dried into a gel at 60 °C. After grinding, the powder was calcined at 250 °C for 3 h and 450 °C for 0.5 h with a heating rate of 2 °C $min^{-1}$. For synthesis of graphene/$MoO_3$ nanosheets composite, 0.1 ml of 20 wt% poly(diallyldimethylammonium chloride) (PDDA) solution was added into 40 mL graphene oxide solution (0.5 mL $mg^{-1}$) and sonicated for 1 h until forming a transparent solution and then the solution was diluted to 100 mL. After that, 200 mg $MoO_3$ nanosheets were dispersed into 100 mL ethanol through sonication. Then, negatively charged $MoO_3$ nanosheets solution was mixed with the above 100 mL positively charged graphene oxide solution and then stirred for an overnight. After filtering, heat treatment was done at 400 °C for 2 h in Ar atmosphere.

### 4.2. Characterization

The surface morphology of the samples was examined by FE-SEM (JSM 700F, JEOL). The microstructure of the samples was investigated by HR-TEM (JEM 2100F, JEOL). The powder sample was sonicated in ethanol for 5 min and the suspension was dropped in a 200 mesh Cu grid. The crystallographic structure of the metal oxides was analyzed by XRD (Rigaku Rotaflex D/MAX System, Rigaku) equipped with Cu K$\alpha$ radiation ($\lambda$ = 0.15406 nm). Raman spectroscopy was performed with a micro-Raman system (Renishaw, RM1000-In Via) with excitation energy of 2.41 eV (514 nm). The surface area was determined by the liquid nitrogen cryosorption (Micromeritics ASAP2020) and the micropore size and mesopore size distribution was calculated by the Horvath-Kawazoe (HK) and Barrett Joyner Halenda (BJH) methods, respectively. TGA (Q500, TA Instrument) was used for the thermal stability analysis, and the temperature was increased by 5 °C/min at $N_2$ atmosphere from room temperature to 1000 °C. The functional group was determined by FT-IR (IFS66/S, Bruker) spectroscopy in the range of 400–4000 $cm^{-1}$.

Electrodes used for fabrication of ASCs were prepared by mixing 80 wt% electroactive material, 15 wt% carbon black, 5 wt% poly (vinylidene fluoride), then a little ethanol was added as solvent. Then the mixture was coated on the nickel foil (diameter 1.1 cm) using doctor blade and dried at 120 °C for 12 h. To construct an ASC, the loading mass ratio of active materials (Gr$MnO_2$//Gr$MoO_3$) was estimated to be 0.78 from the specific capacitance calculated from their CV curves. The electrochemical tests of the individual electrode were performed in a three electrode cell, in which platinum mesh and Ag/AgCl electrode was used as the counter and reference electrodes, respectively. The graphene/$MnO_2$ positive electrode and graphene/$MoO_3$ negative electrode were pressed together and separated by a porous glass carbon filter separator. The electrochemical measurements of the ASCs were carried out in a two electrode cell at room temperature in 1 M $Na_2SO_4$ electrolyte. All of the above electrochemical measurements were carried out by a Biologic VMP3 electrochemical workstation.

## Supporting Information

Supporting Information is available from the Wiley Online Library or from the author. It includes materials, supplementary Table S1, and Figure S1 to S3.

## Acknowledgements

This work was supported by the Research Center Program of Institute for Basic Science (IBS), the World Class University (WCU) program (2008-000-10029-0) of the National Research Foundation of Korea (NRF)

funded by the Ministry of Education, Science and Technology (MEST) of Korea.

Received: May 30, 2013
Published online: August 30, 2013

[1] P. Simon, Y. Gogotsi, *Nat. Mater.* **2008**, *7*, 845.
[2] J. R. Miller, P. Simon, *Science* **2008**, *321*, 651.
[3] H. K. Jeong, M. Jin, E. J. Ra, K. Y. Sheem, G. H. Han, S. Arepalli, Y. H. Lee, *ACS Nano* **2010**, *4*, 1162.
[4] A. Baducci, R. Dugas, P. L. Taberna, P. Simon, D. PLee, M. Mastragostino, S. Passerini, *J. Power Sources* **2007**, *165*, 922.
[5] G. Wang, L. Zhang, J. Zhang, *Chem. Soc. Rev.* **2012**, *41*, 797.
[6] P. J. Hall, M. Mirzaeian, S. I. Fletcher, F. B. Sillars, A. J. R. Rennie, G. O. Shitta-Bey, G. Wilson, A. Cruden, R. Carter, *Energy Environ. Sci.* **2010**, *3*, 1238.
[7] P. C. Chen, G. Shen, Y. Shi, H. Chen, X. Zhou, *ACS Nano* **2010**, *4*, 4403.
[8] Y. G. Wang, Y. Y. Xia, *Electrochem. Commun.* **2005**, *7*, 1138.
[9] Z. Fan, J. Yan, T. Wei, L. Zhi, G. Ning, T. Li, F. Wei, *Adv. Funct. Mater.* **2011**, *21*, 2366.
[10] J. Yan, Z. Fan, W. Sun, G. Ning, T. Wei, Q. Zhang, R. Zhang, L. J. Zhi, F. Wei, *Adv. Funct. Mater.* **2012**, *22*, 2632.
[11] H. Jiang, J. Ma, C. Z. Li, *Adv. Mater.* **2012**, *24*, 4197.
[12] X. Lu, T. Zhai, X. Zhang, Y. Shen, L. Yuan, B. Hu, L. Gong, J. Chen, Y. Gao, J. Zhou, Y. Tong, Z. L. Wang, *Adv. Mater.* **2012**, *24*, 938.
[13] J. Han, L. L. Zhang, S. Lee, J. Oh, K. S. Lee, J. R. Potts, J. Ji, X. Zhao, R. S. Ruoff, S. J. Park, *ACS Nano* **2012**, *7*, 19.
[14] Z. S. Wu, W. Ren, D. W. Wang, F. Li, B. Liu, H. M. Cheng, *ACS Nano* **2010**, *4*, 5835.
[15] H. Gao, F. Xiao, C. B. Ching, H. Duan, *ACS Appl. Mater. Interfaces* **2012**, *4*, 2801.
[16] Z. Wen, X. Wang, S. Mao, Z. Bo, H. Kim, S. Cui, G. Lu, X. Feng, J. Chen, *Adv. Mater.* **2012**, *24*, 5610.
[17] X. Zhao, L. Zhang, S. Murali, M. D. Stoller, Q. Zhang, Y. Zhu, R. S. Ruoff, *ACS Nano* **2012**, *6*, 5404.
[18] C. Liu, Z. Yu, D. Neff, A. Zhamu, B. Z. Jang, *Nano Lett.* **2010**, *10*, 4863.
[19] L. Wei, M. Sevilla, A. B. Fuertes, R. Mokaya, G. Yushin, *Adv. Funct. Mater.* **2012**, *22*, 827.
[20] H. L. Wang, Y. Liang, T. Mirfakhrai, Z. Chen, H. S. Casalongue, H. J. Dai, *Nano Res.* **2011**, *4*, 729.
[21] J. Cheng, M. Sprik, *Phys. Chem. Chem. Phys.* **2012**, *14*, 11245.
[22] V. Chakrapani, C. Pendyala, K. Kash, A. B. Anderson, M. K. Sunkara, J. C. Angus, *J. Am. Chem. Soc.* **2008**, *130*, 12944.
[23] S. Trasatti, *Pure Appl. Chem.* **1986**, *58*, 955.
[24] P. V. Rysselberghe, *Appl. Phys. Lett.* **1953**, *21*, 1550.
[25] M. T. Greiner, M. G. Helander, W. M. Tang, Z. B. Wang, J. Qiu, Z. H. Lu, *Nat. Mater.* **2012**, *11*, 76.
[26] C. A. Pan, T. B. Ma, *Appl. Phys. Lett.* **1980**, *37*, 714.
[27] Z. Viskadourakis, M. L. Parames, O. Conde, M. Zervos, J. Giapintzakis, *Appl. Phys. Lett.* **2012**, *101*, 033505.
[28] F. Chen, R. Schafranek, W. Wu, A. Klein, *J. Phys. D: Appl. Phys.* **2011**, *44*, 1.
[29] M. N. Islam, M. O. Hakim, *J. Mater. Science Lett.* **1986**, *5*, 63.
[30] T. T. Truong, Y. Liu, Y. Ren, L. Trahey, Y. G. Sun, *ACS Nano* **2012**, *6*, 8067.
[31] Y. K. Hsu, Y. C. Chen, Y. G. Lin, L. C. Chen, K. H. Chen, *Chem. Commun.* **2011**, *47*, 1252.
[32] J. S. Lee, K. H. You, C. B. Park, *Adv. Mater.* **2012**, *24*, 1084.
[33] A. Ghosh, E. J. Ra, M. Jin, H. K. Jeong, T. H. Kim, C. Biswas, Y. H. Lee, *Adv. Funct. Mater.* **2011**, *21*, 2541.
[34] F. Yao, F. Güneş, H. Q. Ta, S. M. Lee, S. J. Chae, K. Y. Sheem, C. S. Cojocaru, S. S. Xie, Y. H. Lee, *J. Am. Chem. Soc.* **2012**, *134*, 8646.
[35] K. Fic, G. Lota, M. Meller, E. Frackowiak, *Energy Environ. Sci.* **2012**, *5*, 5842.
[36] Q. Qu, S. B. Yang, X. L. Feng, *Adv. Mater.* **2011**, *23*, 5574.
[37] W. C. Chang, X. Qi, J. C. Kuo, S. C. Lee, S. K. Ng, D. Chen, *CrystEngComm.* **2011**, *13*, 5125.
[38] T. Brezesinski, J. Wang, S. H. Tolbert, B. Dunn, *Nat. Mater.* **2010**, *9*, 146.
[39] W. Tang, L. Liu, S. Tian, L. Li, Y. Yue, Y. Wu, K. Zhu, *Chem. Commun.* **2011**, *47*, 10058.
[40] L. Cai, P. M. Rao, X. L. Zheng, *Nano Lett.* **2011**, *11*, 872.
[41] R. Liang, H. Q. Cao, D. Qian, *Chem. Commun.* **2011**, *47*, 10305.
[42] E. Y. Choi, T. H. Han, J. Hong, J. E. Kim, S. H. Lee, H. W. Kim, S. O. Kim, *J. Mater. Chem.* **2010**, *20*, 1907.
[43] G. R. Li, Z. L. Wang, F. L. Zheng, Y. N. Ou, X. Tong, *J. Mater. Chem.* **2011**, *21*, 4217.
[44] F. Ataherian, N. L. Wu, *J. Electrochem. Soc.* **2011**, *158*, A422.
[45] Q. T. Qu, Y. Shi, S. Tian, Y. H. Chen, Y. P. Wu, R. Holze, *J. Power Sources* **2009**, *194*, 1222.
[46] W. Wang, F. Li, H. M. Cheng, *J. Power Sources* **2008**, *185*, 1563.
[47] J. Zhang, J. Jiang, H. Li, X. S. A. Zhao, *Energy Environ. Sci.* **2011**, *4*, 4009.
[48] M. S. Wu, C. Y. Huang, K. H. Lin, *J. Power Sources* **2009**, *186*, 557.
[49] L. Yuan, X. H. Lu, X. Xiao, T. Zhai, J. Dai, F. Zhang, B. Hu, X. Wang, L. Gong, J. Chen, C. Hu, Y. Tong, J. Zhou, Z. L. Wang, *ACS Nano* **2011**, *6*, 656.
[50] Z. Tang, C. H. Tang, H. A. Gong, *Adv. Funct. Mater.* **2012**, *22*, 1272.
[51] H. Jiang, C. Li, T. Sun, J. Ma, *Nanoscale* **2012**, *4*, 807.
[52] Q. Wang, Z. Wen, J. H. Li, *Adv. Funct. Mater.* **2006**, *16*, 2141.
[53] Z. Lei, J. Zhang, X. S. Zhao, *J. Mater. Chem.* **2012**, *22*, 153.
[54] W. H. Jin, G. T. Cao, J. Y. Sun, *J. Power Sources* **2008**, *175*, 686.
[55] Q. T. Qu, L. Li, S. Tian, W. Guo, Y. P. Wu, R. Holze, *J. Power Sources* **2010**, *195*, 2789.
[56] H. Wang, Q. Gao, J. Hu, *J. Power Sources* **2010**, *195*, 3017.
[57] G. H. Yu, L. B. Hu, N. Liu, H. Wang, M. Vosgueritchian, Y. Yang, Y. Cui, Z. Bao, *Nano Lett.* **2011**, *11*, 4438.
[58] W. S. Hummers, R. E. Offeman, *J. Am. Chem. Soc.* **1958**, *80*, 1339.
[59] Y. T. Chen, F. Guo, A. Jachak, S. P. Kim, D. Datta, J. Y. Liu, I. Kulaots, C. Vaslet, H. D. Jang, J. X. Huang, A. Kane, V. B. Shenoy, H. Robert, *Nano Lett.* **2012**, *12*, 1996.
[60] H. Jiang, T. Sun, C. Li, J. Ma, *J. Mater. Chem.* **2011**, *22*, 2751.